https://doi.org/10.5194/egusphere-2026-5857
Preprint. Discussion started: 9 November 2026
© Author(s) 2026. CC BY 4.0 License.

Cloud fraction driven thermal-infrared radiative effects of Arctic low-level clouds in marine cold air outbreaks

Sophie Rosenburg[1], Benjamin Kirbus[1,a], Anna E. Luebke[1], Michael Schäfer[1], André Ehrlich[1], Marcus Klingebiel[1], Joshua J. Müller[1], and Manfred Wendisch[1]

[1]Leipziger Institut für Meteorologie (LIM), Universität Leipzig, Leipzig, Germany
[a]now at: Fraunhofer-Institut für Energiewirtschaft und Energiesystemtechnik (IEE), Kassel, Germany

Correspondence: Sophie Rosenburg (sophie.rosenburg@uni-leipzig.de)

Abstract. Arctic marine cold air outbreaks (MCAOs) are important meridional air mass transformation events accompanied by spatially extensive cloud formation. Here, the top-of-atmosphere radiative effect of these MCAO clouds is analyzed using airborne thermal-infrared imaging observations conducted during the HALO-$(\mathcal{AC})^3$ research campaign. Based on the capabilities of the high-resolution ($\sim 10\,\mathrm{m}$) imaging, a fine-scale cloud mask is derived. Furthermore, two cloud radiative effects (CREs), an all-sky CRE (including both cloudy and cloud-free areas) and a cloud-only CRE, are quantified. This way, the effects of cloud fraction and cloud properties are separated, and the drivers of the all-sky CRE are evaluated. It is found that the increase of the all-sky CRE downstream in an MCAO is primarily driven by cloud fraction, in particular for a strong MCAO event. In a next step, the approach applicability and its sensitivity to coarser spatial sampling is evaluated by scaling the airborne images down to lower resolutions of satellite observations provided by EarthCARE MSI ($500\,\mathrm{m}$) and Terra/Aqua MODIS ($1000\,\mathrm{m}$). This coarsening results in an underestimation of the CREs, with maximum values found in the strong MCAO case and at MODIS resolution with $-1.9\,\mathrm{W\,m^{-2}}$ (all-sky CRE) and $-2.9\,\mathrm{W\,m^{-2}}$ (cloud-only CRE). The relations between CREs and cloud fraction can still be identified for lower spatial resolutions but lack in robustness. This highlights the importance of high-resolution airborne thermal-infrared imaging in support of large-scale spaceborne cloud observations to determine CREs.

1 Introduction

Clouds play a crucial role in the amplified warming of the Arctic, which is referred to as Arctic amplification (Wendisch et al., 2023). In particular, liquid-water containing clouds persist year-round interacting with atmospheric radiation (Shupe and Intrieri, 2004; Morrison et al., 2012; Kay et al., 2016). The cloud radiative effect (CRE) quantifies this interaction; it can be calculated for the surface and top-of-atmosphere (TOA). In this study, the CRE is analyzed from a TOA-like perspective. The CRE is negative/positive in the solar/thermal-infrared (TIR) spectral ranges indicating a cooling/warming by the clouds at TOA. Therefore, the total CRE (solar plus TIR) depends on the season, surface (sea ice, open ocean) characteristics such as albedo and emissivity, and the cloud macro- and microphysical properties (Shupe and Intrieri, 2004; Becker et al., 2023).

Arctic amplification is most pronounced in winter (Chung et al., 2021). During polar night with no solar radiation available, the TIR warming effect dominates the total CRE. The TIR CRE is driven by cloud emissivity and the altitude of the cloud

https://doi.org/10.5194/egusphere-2026-5857
Preprint. Discussion started: 9 November 2026
© Author(s) 2026. CC BY 4.0 License.

base and top in the local vertical air temperature profile (Webster, 1994; Shupe and Intrieri, 2004; Sedlar et al., 2012). Marine cold air outbreaks (MCAOs) are frequently occurring in winter (Fletcher et al., 2016a; Dahlke et al., 2022; Ran et al., 2026). During MCAOs, cold and dry air moves southwards across the sea ice edge over the warm and moist open ocean surface. MCAOs can extend far to the south, thereby linking the Arctic to often severe weather events in the mid-latitudes (Pithan et al., 2018). Due to the changing atmospheric and surface conditions along the trajectories of MCAOs, the air masses experience significant transformations, which are accompanied by cloud formation and atmospheric boundary layer (ABL) deepening due to enhanced surface heat and moisture fluxes (Lackner et al., 2023; Kirbus et al., 2024; Wendisch et al., 2025). The strength of these fluxes is driven by the temperature contrast between the moving air mass and the surface (Brümmer, 1996; Papritz and Spengler, 2017). During the flow from the sea ice over the open ocean, roll convection often causes the development of cloud streets aligned with the wind direction (Brümmer, 1999; Klingebiel et al., 2026). This process introduces significant inhomogeneities in the macro- and microphysical characteristics of the cloud field and its radiative properties. In the downstream direction, the original stratocumulus field transitions towards open-cell cumulus due to decoupling processes (Brümmer, 1999; Murray-Watson et al., 2023; Paulus et al., 2026). Low-level clouds embedded in an MCAO are often of mixed-phase type with top heights mostly below 4 km (Xia and McFarquhar, 2024). In the initial stages of an MCAO, i.e., the first hours after crossing the sea ice edge, the cloud fraction and cloud top height, as well as the ABL height and cloud liquid water path, increase (Lloyd et al., 2018; Schirmacher et al., 2024). Due to the ABL deepening and the stepwise adjustment of the air mass to the changing surface properties, the temperature at the top of the ABL and the cloud top remain fairly constant. Further downstream, cloud fraction and liquid water path decrease due to roll break-up and precipitation formation (Murray-Watson et al., 2023). The strength of these transformation characteristics aligns with the MCAO intensity. Stronger events favor higher cloud fractions and cloud top heights, deeper ABLs, as well as larger liquid water paths (Murray-Watson et al., 2023; Schirmacher et al., 2024; Xia and McFarquhar, 2024; Weber et al., 2026).

The formation and persistence of cloud streets is still being investigated. It is presumably connected to sea ice edge characteristics, such as inhomogeneities and spatial geometry of the marginal sea ice zone (MIZ) and vertical wind shear (Gryschka et al., 2008; Spensberger and Spengler, 2021; Klingebiel et al., 2025). To resolve the required small spatial scales, large eddy simulations (LES) are initialized with measurements (Juliano et al., 2026; Paulus et al., 2026). Furthermore, weather prediction models and reanalysis products are validated with respect to their realistic representation of processes during MCAOs. Improvements have been made in the model representation of the major features of MCAOs, except for processes close to the surface (Kirbus et al., 2024; Wendisch et al., 2025).

To explore the importance of small-scale cloud inhomogeneities, two-dimensional (2D) imaging observations may serve as a useful tool (Dorff et al., 2022). Thus, dedicated observations are required for the quantification of the CRE along MCAOs. Because the wintertime frequency of MCAOs with weak and moderate intensity has increased in past decades (Ran et al., 2026), TIR radiative measurements are becoming more and more crucial. In the TIR spectral range, the low-level clouds in an MCAO primarily impact the surface radiative energy budget and have a comparably low TOA CRE (Fletcher et al., 2016b). However, these persisting and frequent MCAOs in winter cover an extended area of $500\,\mathrm{km}$ to $2000\,\mathrm{km}$ on a zonal length scale (Fletcher et al., 2016a). This underlines the importance of the downstream development of cloud fraction and cloud properties,

https://doi.org/10.5194/egusphere-2026-5857
Preprint. Discussion started: 9 November 2026
© Author(s) 2026. CC BY 4.0 License.

i.e., cloud top temperature and emissivity, for the CRE from the TOA perspective. Measurements performed by polar-orbiting satellites provide large-scale and long-term data. Radiances measured from space by MODIS (Moderate Resolution Imaging Spectroradiometer) onboard the Terra and Aqua satellites have a spatial resolution of $1\,\mathrm{km}$ for the TIR bands. More recently, the EarthCARE satellite was launched and the onboard Multi-Spectral Imager (MSI, Wehr et al., 2023) measures radiances with $500\,\mathrm{m}$ horizontal spatial resolution. Although restricted in space and time, airborne measurements fill the gap with high spatial and temporal resolution measurements as well as concentrated localized sampling while capturing small-scale characteristics and the radiative impact of the cloud field present during MCAOs.

To analyze the initial downstream development of the TOA CRE and to evaluate its drivers, airborne TIR imaging observations of two MCAO events with different intensities are introduced in Sect. 2 and then analyzed in Sect. 3. First, a cloud mask is defined and a TOA-like CRE is calculated for all pixels (all-sky CRE) and for cloudy pixels only (cloud-only CRE). With this approach the influences of cloud fraction and cloud properties on the TOA-like CRE can be evaluated separately for the two MCAO events. Furthermore, the airborne imaging observations ($\sim 10\,\mathrm{m}$) are scaled down to the spatial resolutions of the spaceborne instruments MSI and MODIS to evaluate the approach applicability to coarser spatial sampling and to state the importance of small-scale resolution and thereby resolved inhomogeneities in the cloud field (Sect. 4). Section 5 sets the results into the context of the methodology and its uncertainties and is followed by conclusions in Sect. 6.

2 Data

2.1 Airborne measurement campaign

The Arctic airborne campaign HALO-$(\mathcal{AC})^3$, conducted in the framework of the "Arctic Amplification: Climate Relevant Atmospheric and Surface Processes, and Feedback Mechanisms" ($(\mathcal{AC})^3$) research project, took place in March and April 2022. The campaign aimed to characterize air mass transformation events such as MCAOs and warm air intrusions following a quasi-Lagrangian sampling strategy (Wendisch et al., 2024). The High Altitude and LOng range research aircraft (HALO; Krautstrunk and Giez, 2012) was equipped to conduct remote sensing measurements over the sea ice, MIZ, and open ocean in the Fram Strait close to Svalbard. The remote sensing payload on the aircraft comprised active as well as passive instruments (Stevens et al., 2019; Ehrlich et al., 2025). In addition, dropsondes were launched to measure vertical air temperature, humidity, and wind profiles (George et al., 2024).

The flight tracks sampling two selected MCAO cases are displayed in Fig. 1 in the context of the $11\,\mu\mathrm{m}$ MODIS brightness temperature image (band 31, MODIS Science Team, 2024). To quantify the intensity of the two MCAOs, the M index is calculated (e.g., Papritz and Spengler, 2017):

$$M = \theta_{\mathrm{SKT,ocean}} - \theta_{850\,\mathrm{hPa}}\,. \tag{1}$$

For this purpose, CARRA (Copernicus Arctic Regional Reanalysis) reanalysis data are used (Schyberg et al., 2021a, b) for the selected sections (dot markers in Fig. 1) covering open ocean area with $\theta_{\mathrm{SKT,ocean}}$ and $\theta_{850\,\mathrm{hPa}}$ being the potential ocean skin temperature and the potential temperature at $850\,\mathrm{hPa}$. The flight on 30 March 2022 sampled a weak MCAO with a mean

https://doi.org/10.5194/egusphere-2026-5857
Preprint. Discussion started: 9 November 2026
© Author(s) 2026. CC BY 4.0 License.

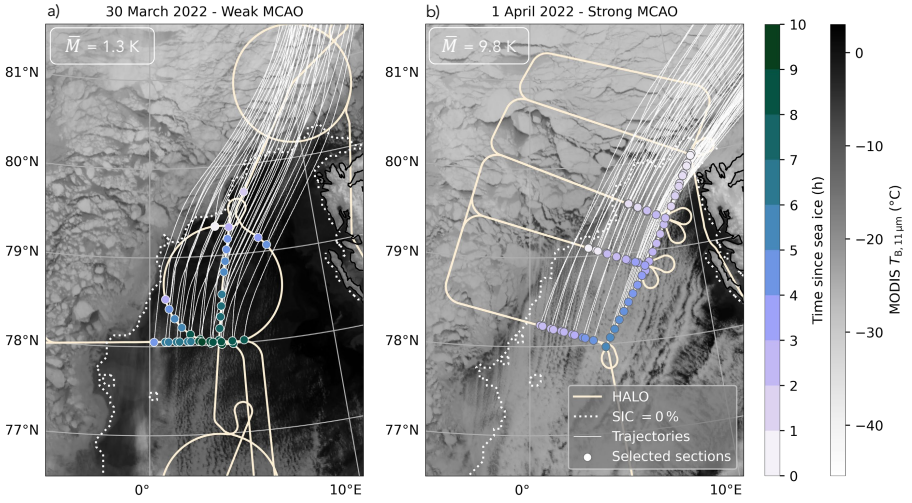


Figure 1. Case overview. HALO flight tracks on **(a)** 30 March 2022 and **(b)** 1 April 2022 as solid beige lines with backward trajectories as thin white lines. Locations of selected VELOX pushbrooms, which coincide with starting points of the backward trajectories, are marked by circles and are colored by the time since the air mass crossed the sea ice edge. Sea ice concentration of 0 % (AMSR2; Spreen et al., 2008) is indicated as a dotted white contour line. MODIS 11 µm brightness temperature (band 31, MOD021KM, MODIS Science Team, 2024) is shown in the background. The respective mean MCAO index M of the analyzed sections is given in the upper left corner.

M of 1.3 K. In contrast, a strong event with a mean M about 9.8 K was captured on 1 April 2022, which is characterized by a higher cloud fraction and more defined cloud streets in the MODIS brightness temperature image.

2.2 Selection of flight sections based on backward trajectories

To mimic the air mass transformations of individual air parcels crossing the flight path, trajectories are calculated 24 hours backwards using the Lagrangian Analysis Tool (LAGRANTO; Sprenger and Wernli, 2015) and ERA5 wind fields (Hersbach et al., 2020). Dropsonde measurements performed during the HALO-$(AC)^3$ campaign are assimilated into the reanalysis data, thereby improving its reliability (Kirbus et al., 2024). The backward trajectories start every minute from the HALO flight track at a height of 920 hPa, which is close to cloud tops in the proximity of the sea ice edge and, therefore, should be unaffected by surface effects. In addition, the sea ice concentration (SIC) is tracked along the trajectories using the spaceborne dataset from AMSR2 (Advanced Microwave Scanning Radiometer - 2; Spreen et al., 2008). Therefore, the time the air mass spent over open ocean since crossing the sea ice edge, here defined at SIC = 0 %, is calculated. This will be used as the metric "time since sea ice" in the following.

The trajectories and SIC = 0 % are used to select flight sections over open ocean. Furthermore, only sections with a latitude greater than 78°N are considered as the flight track on the 1 April 2022 does not extend further south in the region of interest. Data collected with aircraft pitch and roll angles greater than 6° are filtered out to avoid sharp turns. For the observations collected on 30 March 2022, part of the trajectories cross over Svalbard. To avoid the influence of orography, the affected

https://doi.org/10.5194/egusphere-2026-5857
Preprint. Discussion started: 9 November 2026
© Author(s) 2026. CC BY 4.0 License.

sections of the flight track are excluded from the analysis. In Fig. 1, the starting points of the remaining trajectories are indicated by filled dot markers colored by time since the air parcel crossed the sea ice edge. To reach the latitude of 78°N, the air masses need about 9 to 10 hours on 30 March 2022, whereas on 1 April 2022 a similar distance is traveled by the air parcel in 5 to 6 hours. This difference is confirmed by horizontal wind speeds in the CARRA reanalysis. The mean horizontal wind speed at 850 hPa is about $11.0\,\mathrm{m\,s^{-1}}$ for the stronger MCAO event on 1 April 2022 and $5.3\,\mathrm{m\,s^{-1}}$ during the weaker event on 30 March 2022 for the respective selected flight sections. This relation between MCAO intensity and wind speed was already reported by Kolstad (2017).

2.3 Thermal-infrared imaging observations

The thermal-infrared imager VELOX (Video airbornE Longwave Observations within siX channels; Schäfer et al., 2022) measures two-dimensional (2D) fields of brightness temperatures, T_B, of surfaces and cloud tops in two redundant broadband channels and four spectral channels in the atmospheric window region from 7.7 µm to 12 µm. To cover a larger spectral range, the broadband channel (7.7 – 12 µm) with 1 Hz temporal resolution and a noise equivalent temperature difference (NETD) of 48 mK is used here (Schäfer et al., 2023). VELOX has a field of view of 35.5° x 28.7° with 640 x 512 pixels in the across- and along-track direction, respectively. For a target distance of 10 km, the spatial resolution is about 10 m x 10 m per pixel. The high spatial resolution allows for identification of small-scale cloud structures as shown by the example image in Fig. 2a. These images are the basis for the cloud mask definition (Sect. 3.1). For the following CRE analysis (Sect. 3.2), the central stripes of the brightness temperature fields are extracted and merged together along the flight track. These pushbroom-like images do not suffer from effects of slanted viewing angles in flight direction and do not overlap each other. In the across-track direction, a maximum viewing zenith angle of 17.75° is reached. A sensitivity study based on radiative transfer simulations with the libRadtran (library for Radiative transfer) software package (Emde et al., 2016) yields a brightness temperature difference of −0.1 K for edge pixels compared to nadir. This deviation is rather small, but will be considered during the following analysis. Each pushbroom image covers 1 min of flight time, which translates into a distance of about 12 km along the flight track. The pushbrooms are centered at the starting locations of the backward trajectories. These are indicated by the filled dots in Fig. 1, which are colored by time since sea ice. Close to the MIZ, contamination with sea ice is likely. In the TIR wavelength range, sea ice and clouds may have similar brightness temperatures making a distinction difficult. The pushbroom images are inspected visually and are discarded in case of clear indications of sea ice contamination. Especially for the weak MCAO case on 30 March 2022, thin sea ice areas are detected over the ocean in 18 pushbroom images. In the case of the strong MCAO event, only two pushbrooms are excluded. In total, 37 and 62 pushbroom images are analyzed for the weak and the strong MCAO case, respectively.

https://doi.org/10.5194/egusphere-2026-5857
Preprint. Discussion started: 9 November 2026
© Author(s) 2026. CC BY 4.0 License.

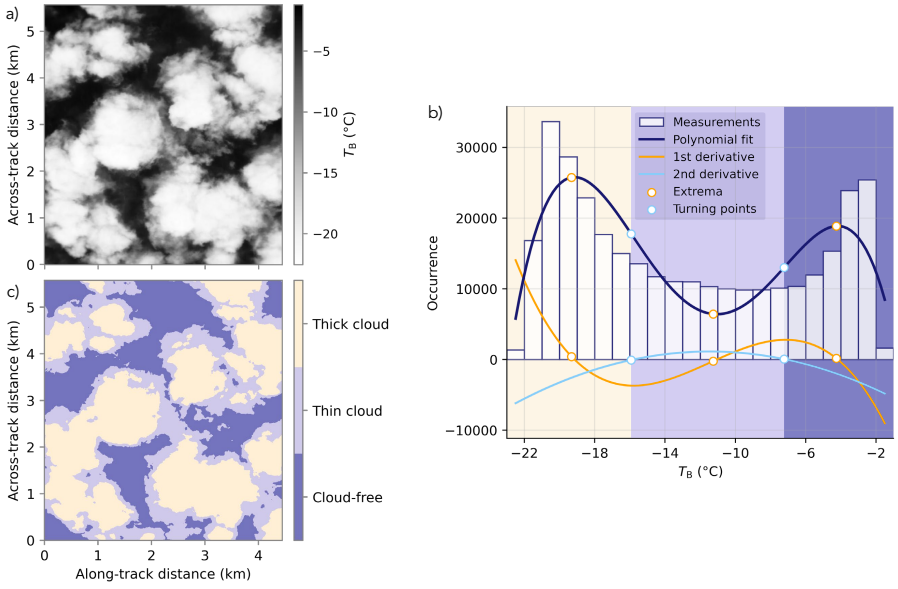


Figure 2. **(a)** Example VELOX broadband brightness temperature field (strong MCAO on 1 April 2022, northernmost horizontal leg over open ocean). **(b)** Brightness temperature histogram of **(a)** with fitted 4th order polynomial and its first and second derivatives as well as its extrema and turning points, which indicate the classes cloud-free (dark violet), thin cloud (light violet), thick cloud (beige). **(c)** Deduced cloud mask.

3 Methods

3.1 Cloud mask

A new cloud mask is constructed to classify the single pixels and to determine cloud fractions. The brightness temperature field in Fig. 2a shows a typical cloud distribution of cloud streets. Three categories can be identified: cloud-free open ocean, thin and thick cloud parts. The thin cloud parts are identified at cloud edges, at which clouds are optically thinner and the measured brightness temperature at flight level is composed of the emission by the ocean surface and the thin cloud. Optically thick cloud pixels are usually located in the cloud center, where the cloud is emitting like a black body. These categories are reflected in the bimodality of the histogram shown in Fig. 2b (based on data in Fig. 2a) with one mode at lower brightness temperature values (thick cloud), one at larger brightness temperature values (cloud-free open ocean) and the range in between, which belongs to the thin cloud class.

To define general brightness temperature thresholds applicable for cloud regimes captured during a whole flight, all VELOX images showing a bimodal brightness temperature distribution (including ocean surface and clouds; 62 images for the weak MCAO, 123 images for the strong MCAO case) are analyzed separately. For this purpose, the original VELOX images are used as the captured area (about $6.4\,\mathrm{km} \times 5.1\,\mathrm{km}$ for a target distance of $10\,\mathrm{km}$) does show more isolated cloud scenes. For each of these images, the thresholds are derived with the following procedure: (i) A 4th order polynomial function is fitted to the

https://doi.org/10.5194/egusphere-2026-5857
Preprint. Discussion started: 9 November 2026
© Author(s) 2026. CC BY 4.0 License.

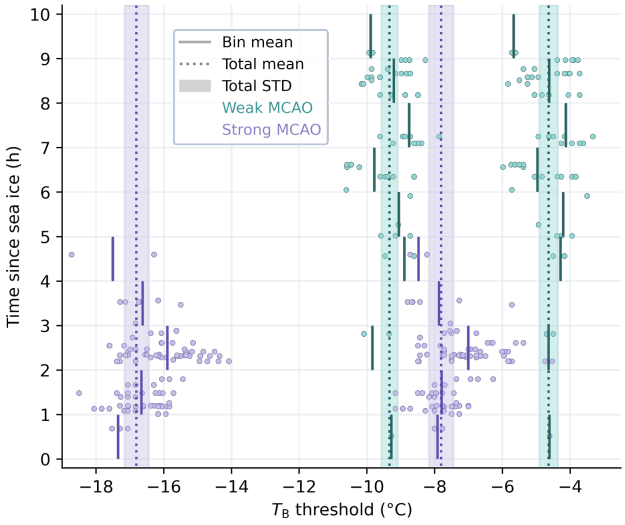


Figure 3. Cloud mask brightness temperature thresholds as dots for VELOX brightness temperature fields (selected according to Sect. 3.1) sorted by time since sea ice for the weak MCAO (teal) and strong MCAO (violet). The means of 1 h time since sea ice bins are shown as solid lines. Dotted lines and shading represent mean and standard deviation (STD) of the bin means.

brightness temperature distribution. (ii) The two turning points of this function are computed by determining the zero crossings of its second derivative as exemplarily shown in Fig. 2b. (iii) These turning points are used as the cloud mask threshold values, where the lower threshold defines the distinction between the thick and thin cloud classes and the upper threshold separates the thin cloud and cloud-free class. As an example, the application of these thresholds is shown in Fig. 2c. Figure 3 shows the derived thresholds for the individual images, which are sorted into hourly time since sea ice bins. For each bin, the mean of the lower and upper threshold is calculated. These bin means of the thresholds fall within a rather small brightness temperature range and do not show a clear relation to the time since sea ice. This justifies the decision to define a cloud mask applicable to a whole flight. Therefore, the mean and standard deviation of these bin means are computed resulting in the applicable cloud mask for the respective flight. The standard deviations are used in a cloud mask sensitivity study in Sect. 5 and App. A.

It is evident that the thresholds are lower for the strong MCAO case on 1 April 2022 than for the weak event on 30 March 2022. Cloud tops are therefore higher and colder for the stronger MCAO, which was also shown by Weber et al. (2026). As depicted in the satellite images in Fig. 1, the weaker MCAO favors low cloud fraction conditions whereas the strong event is characterized by high ones.

3.2 Thermal-infrared cloud radiative effects

The cloud radiative effect is calculated pixel-wise following the independent column approximation similar to Eytan et al. (2020) for each VELOX pushbroom image. The brightness temperatures, T_B, measured by VELOX were converted to irradiances for each pixel (x, y). First, T_B is converted to a radiance, B, using the Planck formula and spectrally integrated over

https://doi.org/10.5194/egusphere-2026-5857
Preprint. Discussion started: 9 November 2026
© Author(s) 2026. CC BY 4.0 License.

the wavelength range, λ, of the broadband channel $7.7\,\mu\mathrm{m}$ to $12.0\,\mu\mathrm{m}$. Isotropy is assumed leading to a radiance-to-irradiance conversion by multiplying with π:

$$F(T_\mathrm{B},x,y) = \pi \cdot \int_{7.7\,\mu\mathrm{m}}^{12\,\mu\mathrm{m}} B(\lambda,T_\mathrm{B},x,y)\,\mathrm{d}\lambda. \tag{2}$$

The resulting irradiance, $F(T_\mathrm{B},x,y)$, is given in units of $\mathrm{W\,m^{-2}}$.

The CRE, $\Delta F(T_\mathrm{B},x,y)$, is defined as the difference of the cloud-free reference irradiance, $F(T_\mathrm{B},x,y)_\mathrm{cloud\text{-}free}$, and the irradiance of the cloudy state, $F(T_\mathrm{B},x,y)_\mathrm{cloudy}$. The result can be interpreted as a spatially highly resolved CRE at flight altitude, i.e., corresponding to a TOA-like perspective if no clouds were above the aircraft:

$$\Delta F(T_\mathrm{B},x,y) = F(T_\mathrm{B},x,y)_\mathrm{cloud\text{-}free} - F(T_\mathrm{B},x,y)_\mathrm{cloudy}. \tag{3}$$

The cloud-free state needed as a reference to calculate the CRE is directly derived from the VELOX measurements. For each of the two MCAO cases, the 95th percentile irradiance of the pixels, which are classified as cloud-free, is set as the cloud-free reference. This approach allows comparability of the different pushbroom sections for the respective case.

Due to the isotropy assumption, the irradiances are overestimated by neglecting the longer pathway through the atmosphere for off-nadir directions. The impact on the resulting CRE is quantified by radiative transfer simulations with libRadtran using the atmospheric profiles measured by dropsondes. A mean CRE overestimation of $0.08\,\mathrm{W\,m^{-2}}$ is determined for the weak MCAO case while $0.8\,\mathrm{W\,m^{-2}}$ is determined for the strong MCAO case. In the strong MCAO event, the imbalance in path length of the cloud-free and cloudy states is larger as this MCAO featured higher cloud tops. In addition, the impact of the angular brightness temperature deviation in the across-track direction of $-0.1\,\mathrm{K}$ on the CRE is also estimated. The effect depends on the pixel brightness temperature and is at its maximum for the cloud-free state and about $-0.16\,\mathrm{W\,m^{-2}}$. Therefore, while the effects of assuming isotropy for the radiance-irradiance conversion and of larger viewing zenith angles should be considered they do not disturb the results of the following analysis, in which pushbroom mean CREs are used.

Based on the retrieved CRE fields, the cloud-only CRE, $\Delta F_\mathrm{cloud\text{-}only}$, and the all-sky CRE, $\Delta F_\mathrm{all\text{-}sky}$, are distinguished. The cloud-only CRE is defined as the radiative effect of the cloudy pixels of a pushbroom-like image (only the thick cloud class of the cloud mask is used) and thus is independent of cloud fraction. The cloud-only CRE is limited to the thick cloud pixels, which enables to estimate the maximum possible radiative effect of these clouds by filtering out the thin cloud pixels at the cloud edges. The all-sky CRE is the radiative effect of all pixels (cloud-free, thin cloud, and thick cloud pixels) in a pushbroom image. Thus, the all-sky CRE is determined by the cloud properties, but also by cloud fraction. Figure 4a to 4c show an example VELOX pushbroom image, the applied cloud mask, and the CRE calculated for all pixels of the pushbroom, i.e., the all-sky CRE. The pixels classified as cloud-free or thin cloud by the cloud mask are hatched to highlight the CRE of the thick cloud pixels, i.e., the cloud-only CRE. The two types of CRE allow for an analysis of the CRE drivers and the separation of the impact of cloud properties from cloud fraction.

https://doi.org/10.5194/egusphere-2026-5857
Preprint. Discussion started: 9 November 2026
© Author(s) 2026. CC BY 4.0 License.

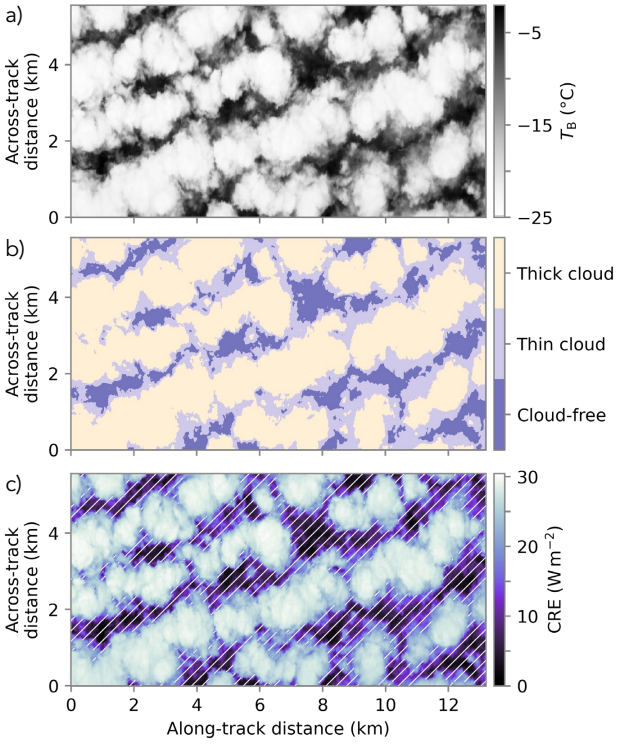


Figure 4. **(a)** VELOX pushbroom image in the broadband channel with applied cloud mask in **(b)** and pixel-wise calculated CRE in **(c)**, where areas with pixels classified as thin cloud or cloud-free by the cloud mask are hatched.

4 Results and discussion

4.1 Cloud fraction and cloud top brightness temperature

The weak and strong MCAO cases are characterized by contrasting cloud conditions. For the weak MCAO, accumulated over all analyzed pushbrooms about $67.6\,\%$ of the pixels are cloud-free while only $23.7\,\%$ and $8.7\,\%$ are classified as thin and thick cloud, respectively. In contrast, the majority of pixels from the strong MCAO are in the thick cloud class ($67.7\,\%$), $20.9\,\%$ are in the thin cloud class, and about $11.4\,\%$ are cloud-free.

To analyze these contrasts in more detail, Fig. 5a and 5c present the downstream evolution of the total cloud fraction (thin plus thick cloud fraction) as mean values for hourly time since sea ice bins. In both MCAOs, the total cloud fraction increases after a certain time since sea ice and reaches its maximum at the greatest temporal distance to the sea ice edge. However, the total cloud fraction is rather variable for the first hours after crossing the sea ice edge during the weak MCAO because only one pushbroom could be analyzed for these bins. For the strong MCAO case, the total cloud fraction is generally high with a slight decrease in the 1-2 hours since sea ice bin. This could be explained by a lee effect of Svalbard (see MODIS image in

https://doi.org/10.5194/egusphere-2026-5857
Preprint. Discussion started: 9 November 2026
© Author(s) 2026. CC BY 4.0 License.

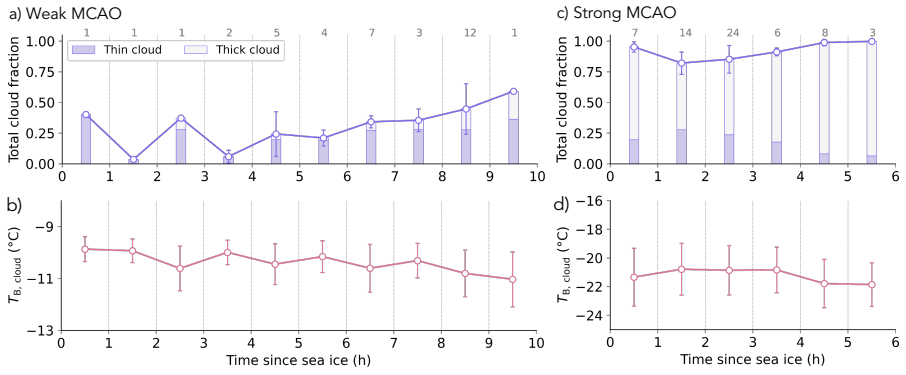


Figure 5. Downstream development of total cloud fraction (thin plus thick cloud fraction; top panels) and cloud top brightness temperature (thick cloud pixels; bottom panels) $T_{\mathrm{B,\,cloud}}$ **(a)**, **(b)** during the weak MCAO and **(c)**, **(d)** for the strong MCAO. Pushbrooms were sorted into 1 h bins of time since sea ice. Bin means and standard deviations are displayed. Gray numbers at the top state the number of pushbroom images in each bin.

Fig. 1b). For both MCAO cases, the thick cloud fraction increases while the thin cloud fraction remains constant or decreases in the downstream direction as larger cloud clusters develop and less thin cloud edges are present.

Figures 5b and 5d illustrate the downstream development of the mean brightness temperature of the thick cloud pixels per bin. Comparing the two MCAO cases, the mean cloud top brightness temperature is lower for the stronger event and ranges between $-22\,^{\circ}\mathrm{C}$ and $-21\,^{\circ}\mathrm{C}$. The weaker event features cloud tops with brightness temperatures about $-11\,^{\circ}\mathrm{C}$ to $-10\,^{\circ}\mathrm{C}$. Murray-Watson et al. (2023) showed that more intense MCAO events have higher and colder cloud tops. Weber et al. (2026) determined the cloud top height for both regarded cases (see their Fig. 5a) and found that higher cloud top heights were observed for the strong MCAO on 1 April 2022 (up to 1500 m) than for the weak MCAO on 30 March 2022 (up to 750 m) in the initial hours since crossing the sea ice edge. Although a small downstream decrease is observed, the mean cloud top brightness temperature remains fairly constant due to the vertical extension of the ABL in the initial stages of the MCAO, as it was also reported by Murray-Watson et al. (2023).

4.2 Thermal-infrared cloud radiative effects

The downstream evolution of the CREs is presented in Fig. 6. The selected pushbrooms are again sorted into hourly bins of time since sea ice and their all-sky and cloud-only CRE distributions are shown. The all-sky CRE distributions for the weak MCAO have their dominant mode at low values reflecting the low cloud fraction. In contrast, the all-sky and cloud-only CRE distributions for the strong MCAO show almost identical distributions for each bin, highlighting the thick cloud regime as dominant. The variability and multimodality in the distributions is caused by the sampling statistics and local variations.

The general magnitude of the cloud-only CRE is almost twice as high for the stronger MCAO case compared to the weaker event. This is supported by the colder cloud tops characteristic for the strong MCAO (Fig. 5d).

https://doi.org/10.5194/egusphere-2026-5857
Preprint. Discussion started: 9 November 2026
© Author(s) 2026. CC BY 4.0 License.

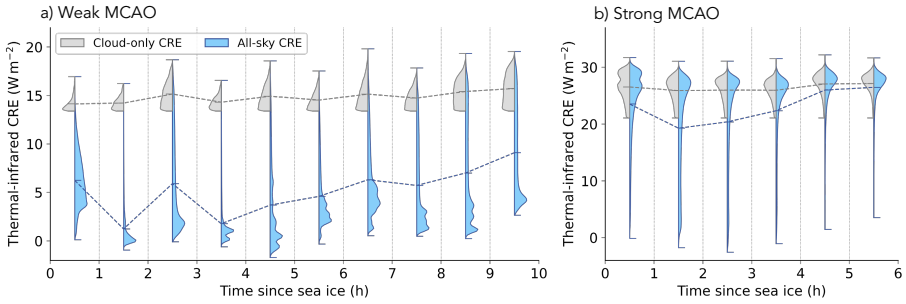


Figure 6. Downstream development of cloud-only (grey) and all-sky CRE (light blue) **(a)** for the weak MCAO and **(b)** for the strong MCAO case. The pushbroom images were sorted into 1 h time since sea ice bins. Bin distributions are shown as violins, bin means are indicated and connected by dashed lines.

In addition, the mean CRE of each bin is indicated. The mean cloud-only CRE is rather stable for both cases whereas the mean of the all-sky CRE increases with time since sea ice. The cloud-only CRE depends solely on the cloud properties whereas the all-sky CRE encompasses both, the cloud fraction and properties. This indicates that the microphysical properties of the clouds themselves do not change distinctly with increasing time since sea ice whereas the cloud fraction is driving the all-sky CRE increase.

To elaborate on the dependence of the CREs on cloud fraction, Fig. 7 shows the mean all-sky and cloud-only CRE in relation to the total cloud fraction for all pushbrooms for the two MCAO cases, respectively. Although the cases capture two different cloud fraction regimes, the relations are found to be linear and a linear function is fitted. In the case of the all-sky CRE, the coefficients of determination R^2 for the fit are high with 0.95 and 0.93 for the weak and strong MCAO, respectively. R^2 is lower for the cloud-only CRE with values of about 0.70 and 0.62 for the two cases. Although the cloud-only CRE is solely dependent on cloud emissivity and cloud top temperature, a nonlinear emissivity increase for critical optical thicknesses below 10 cannot be ruled out, even with the consideration of thick cloud pixels only. Thus, it is possible that the relation shown here implicates a nonlinearity, but additional information is needed to confirm this.

The sensitivity of the CRE to cloud fraction is naturally higher for the all-sky CRE than for the cloud-only CRE. The change of cloud-only CRE with cloud fraction indicates that cloud properties, i.e., cloud top temperature and emissivity, also change with cloud fraction and, therefore, within the downstream air mass transformation. The slope of the cloud-only CRE function would be close to unity in the case of clouds that are not changing. However, Weber et al. (2026) report a downstream increase in effective radius of liquid water droplets at cloud top, and Murray-Watson et al. (2023) show an increase in liquid water path. For the cloud optical thickness, these changes would counteract and imply a limited change in emissivity. Furthermore, the cloud top temperature shown in Fig. 5b and d remains fairly constant. Thus, the cloud-only CRE is only increasing weakly with higher cloud fraction, which can also be interpreted as a proxy for the time since sea ice in this context.

As both factors, cloud fraction and cloud properties, are combined in the all-sky CRE, it is concluded that the all-sky CRE is mainly driven by cloud fraction and only weakly by changing cloud properties. In addition, the sensitivity, i.e., the slope of

https://doi.org/10.5194/egusphere-2026-5857
Preprint. Discussion started: 9 November 2026
© Author(s) 2026. CC BY 4.0 License.

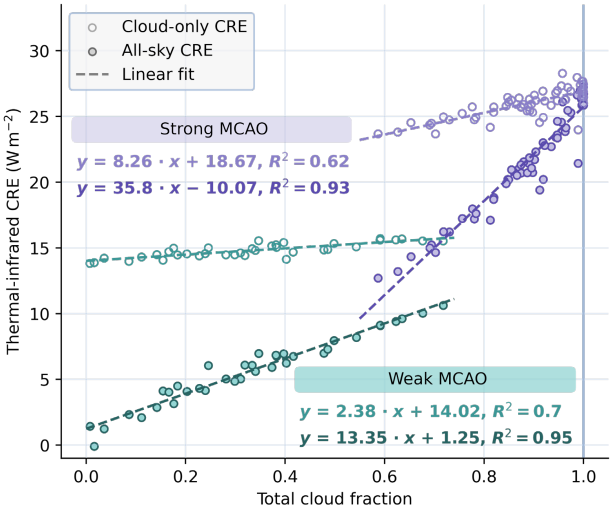


Figure 7. Pushbroom mean all-sky and cloud-only CRE as a function of total cloud fraction (thin plus thick cloud fraction). A linear fit is applied, the respective linear functions and the coefficient of determination R^2 are given for both MCAO cases.

the linear function, of $35.80\,\mathrm{W\,m^{-2}}$ for the strong MCAO is almost three times larger than the slope of $13.35\,\mathrm{W\,m^{-2}}$ for the weak MCAO.

The intercept of the linear function describing the all-sky CRE for the strong MCAO is rather large and negative. While this statement may imply a less robust extrapolation to low cloud fractions, the negative number could also be explained by a potential underestimation of the all-sky CRE. For the strong MCAO case, only $11.4\,\%$ of all pixels are classified as cloud-free and might be contaminated by thin cloud parts. Therefore, the selected cloud-free reference could be underestimated as it will be discussed in Sect. 5.2.

4.3 Applicability to coarser spatial sampling

To evaluate the approach applicability and the sensitivity of cloud fraction, CREs and their relation regarding the spatial resolution of the TIR imaging observations, the resolution of the VELOX pushbrooom images ($\sim 10\,\mathrm{m}$) is scaled down to EarthCARE MSI ($500\,\mathrm{m}$) and Terra/Aqua MODIS ($1000\,\mathrm{m}$) spatial resolutions. For this purpose, the VELOX pushbrooms are cut to whole kilometers to accommodate a fair comparison between all resolutions. Figure 8 shows an example pushbroom that captures cloud street structures during the strong MCAO at these different spatial resolutions. It is evident that the cloud-free gaps between the cloud streets become less distinct and that brightness temperature contrasts diminish for coarser spatial resolutions. This is also reflected in the pixel classification by the VELOX cloud mask, which is shown for the two MCAO cases in Fig. 9. As a result of areal averaging with decreasing spatial resolution, the cloud-free and thick cloud fraction are decreasing while the thin cloud fraction is increasing.

https://doi.org/10.5194/egusphere-2026-5857
Preprint. Discussion started: 9 November 2026
© Author(s) 2026. CC BY 4.0 License.

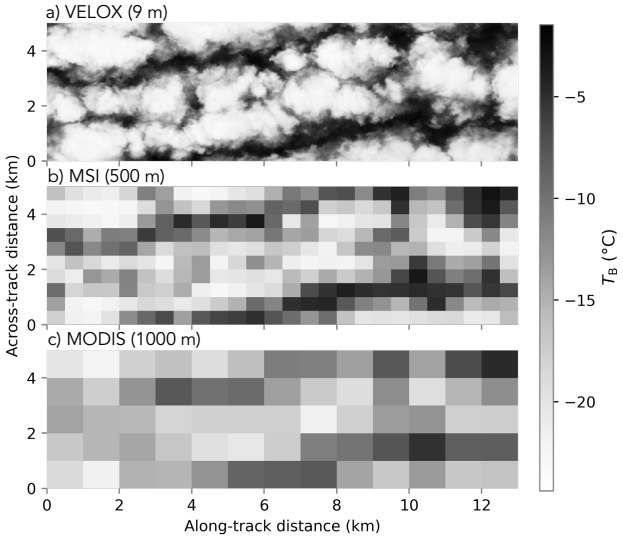


Figure 8. (a) VELOX pushbroom image, showing cloud streets during the strong MCAO event on 1 April 2022, scaled down to **(b)** MSI and **(c)** MODIS resolutions.

Furthermore, the change in total cloud fraction due to resolution is analyzed in Fig. 10a. For low total cloud fractions, the coarser MSI and MODIS resolutions yield an underestimation, which is caused by averaging over primarily cloud-free and sparsely occurring cloudy VELOX pixels. A turning point is reached with increasing total cloud fraction, and for total VELOX cloud fractions larger than 0.3, an overestimation is found for lower resolutions. Here, the increasing occurrence of cloudy VELOX pixels is causing a loss in cloud-free area. Therefore, for the MODIS resolution overcast conditions are already reached for a VELOX total cloud fraction close to 0.85.

Similarly, the derived pushbroom mean all-sky and cloud-only CREs are compared for different spatial resolutions in Fig. 10b and Table 1. A general underestimation in the CREs derived from the coarser resolutions is found, which varies depending on MCAO case and spatial resolution. The underestimation in the all-sky CRE is mainly caused by the change in the cloud-free reference irradiance and only weakly by the single pixel irradiance. As described in Sect. 3, the 95th percentile of the cloud-free pixel irradiance is chosen as the reference. With scaling down the spatial resolution by areal averaging, this cloud-free reference decreases. This effect is amplified for the strong MCAO due to the smaller cloud-free fraction of pixels and, therefore, potential contamination by cloudy pixels while averaging. Thus, the mean MSI/MODIS all-sky CRE bias is $-0.25/-0.30\,\mathrm{W\,m^{-2}}$ for the weak MCAO case and $-0.72/-1.86\,\mathrm{W\,m^{-2}}$ for the strong MCAO.

The cloud-only CRE at MSI and MODIS resolutions is also lower than the VELOX CRE. Other than the impact of the cloud-free reference, irradiances of the thick cloud pixels are also affected by scaling down the resolution. In general, the thick cloud irradiance is increasing for lower resolutions, i.e., the cloud tops are warmer. Consequently, the cloud-only CRE is underestimated with a mean MSI/MODIS bias of $-0.76/-1.26\,\mathrm{W\,m^{-2}}$ for the weak MCAO case and with $-1.22/-2.90\,\mathrm{W\,m^{-2}}$ for the strong MCAO.

https://doi.org/10.5194/egusphere-2026-5857
Preprint. Discussion started: 9 November 2026
© Author(s) 2026. CC BY 4.0 License.

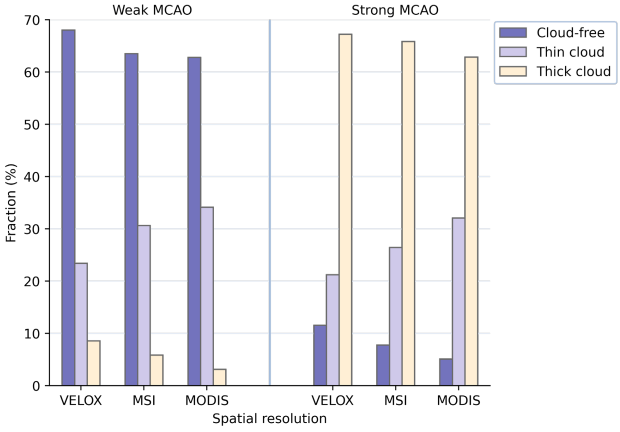


Figure 9. Cloud-free, thin and thick cloud fractions for the different spatial resolutions accumulated for all analyzed pushbrooms during the weak and strong MCAO.

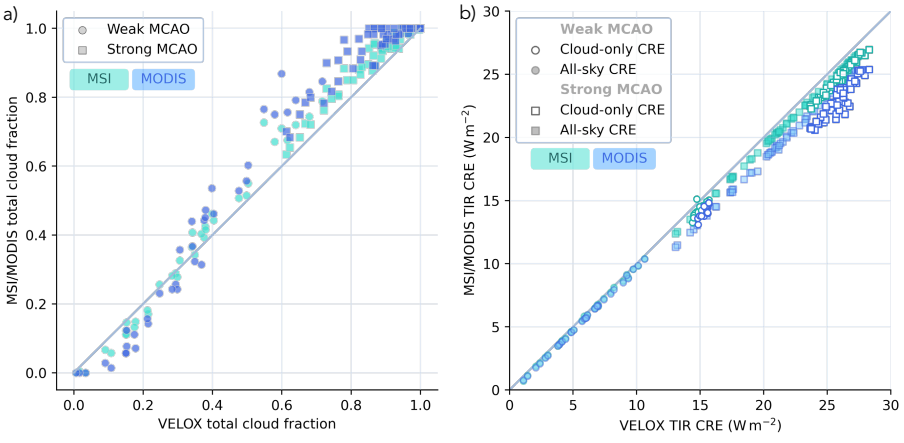


Figure 10. (a) Comparison of total cloud fractions (thin plus thick cloud fraction) for different spatial resolutions (MSI - turquoise, MODIS - blue) and MCAO cases (weak MCAO - dots, strong MCAO - squares). **(b)** Comparison of all-sky (filled markers) and cloud-only (open markers) CREs.

In summary, Fig. 11 shows the relation of CREs and total cloud fraction for the different resolutions. Similar to Fig. 7, the relations are fitted with a linear function. The respective functions and the coefficients of determination are given in Table 1. The increasing underestimation of both CREs with decreasing resolution is seen here once again. There is a transition from underestimated total cloud fraction for very low cloud fractions to an overestimation for higher cloud fractions, which is especially visible for the weak MCAO case featuring mostly cloud-free scenes (Fig. 11a). Otherwise, the general shift from VELOX CREs and total cloud fractions to MSI and MODIS equivalents is directed to lower CREs and higher total cloud

https://doi.org/10.5194/egusphere-2026-5857
Preprint. Discussion started: 9 November 2026
© Author(s) 2026. CC BY 4.0 License.

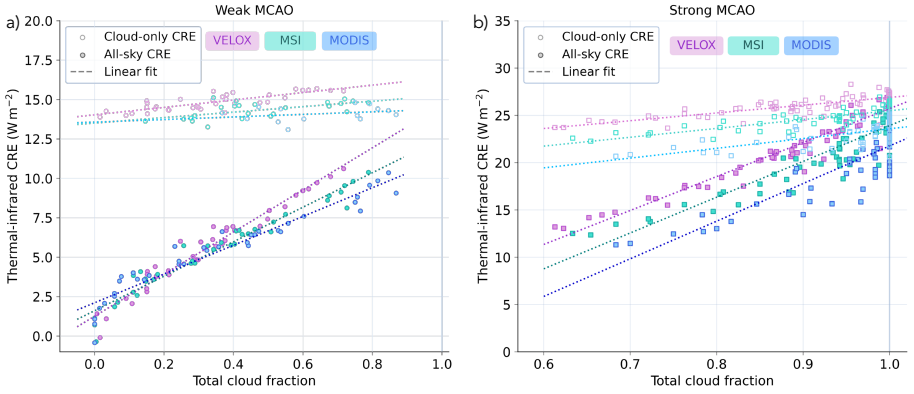


Figure 11. Pushbroom mean all-sky (saturated colors, filled markers) and cloud-only (pastel colors, open markers) CREs as a function of total cloud fraction (thin plus thick cloud fraction) for VELOX (pink), MSI (turquoise) and MODIS (blue) resolutions for **(a)** the weak MCAO and **(b)** strong MCAO. Fitted linear functions and coefficients of determination R^2 can be found in Table 1. Please be aware of the different axes scaling.

fractions. However, the overall relation between cloud fractions and all-sky CRE as well as cloud-only CRE is still represented, though it is less robust for coarser resolutions as expressed by the decrease of the coefficient of determination.

5 Analysis of uncertainties

5.1 Cloud mask

The new cloud mask developed here relies on two thresholds, which are determined statistically as a mean value. To evaluate the sensitivity of the main result (see Fig. 7) to changes in these thresholds, their standard deviations (see Fig. 3) are added and subtracted (see Appendix A). It is found that the slopes and intercepts are changing slightly on the order of $1\,\mathrm{W\,m^{-2}}$ to $2\,\mathrm{W\,m^{-2}}$. However, the results for the all-sky CRE tend to converge for low and high cloud fractions, reaching states in which pixels are clearly cloud-free or thick cloud, independent of the threshold shift. These shifts only matter in the intermediate range of cloud fractions. Here, the uncertainty caused by the cloud mask is highest due to more cloud edges. However, a linear relationship between all-sky CRE and cloud fraction in the regarded cloud fraction regimes is evident and robust. It appears reasonable to apply one set of thresholds for a whole flight as the emission of the clouds is not changing much with time since sea ice as shown in Fig. 5. The use of observations at coarser spatial resolutions further compounds the possible impact of cloud mask thresholds and their derivation. As shown in Fig. 10a the impact of coarser spatial resolution is reflected in cloud fractions skewed to the dominant state in the area of interest, i.e., cloud-free or cloudy. The analyses are based on the cloud mask thresholds that are derived with bimodal brightness temperature distributions captured by the high resolution airborne imaging by VELOX. This gives rise to the question, could spaceborne measurements with coarser resolution be able to resolve this bimodality and apply a similar cloud masking method?

https://doi.org/10.5194/egusphere-2026-5857
Preprint. Discussion started: 9 November 2026
© Author(s) 2026. CC BY 4.0 License.

Table 1. Comparison of all-sky CRE, cloud-only CRE and their relation to total cloud fraction for different spatial resolutions of the airborne VELOX and the spaceborne MSI and MODIS instruments. Mean biases are given as the mean differences between pushbroom mean MSI/-MODIS CRE and VELOX CRE. The linear functions are describing the relation of CRE (y, in $\mathrm{W\,m^{-2}}$) and total cloud fraction (x).

	VELOX ($\sim 10\,\mathrm{m}$)	MSI ($500\,\mathrm{m}$)	MODIS ($1000\,\mathrm{m}$)
Weak MCAO			
All-sky CRE			
Mean bias ($\mathrm{W\,m^{-2}}$)	-	-0.25	-0.30
Function, R^2	$y = 13.36 \cdot x + 1.26;\ 0.96$	$y = 10.94 \cdot x + 1.61;\ 0.95$	$y = 9.12 \cdot x + 2.11;\ 0.92$
Cloud-only CRE			
Mean bias ($\mathrm{W\,m^{-2}}$)	-	-0.76	-1.26
Function, R^2	$y = 2.35 \cdot x + 14.03;\ 0.68$	$y = 1.73 \cdot x + 13.51;\ 0.37$	$y = 0.82 \cdot x + 13.57;\ 0.08$
Strong MCAO			
All-sky CRE			
Mean bias ($\mathrm{W\,m^{-2}}$)	-	-0.72	-1.86
Function, R^2	$y = 35.89 \cdot x - 10.18;\ 0.93$	$y = 37.84 \cdot x - 13.92;\ 0.83$	$y = 39.77 \cdot x - 18.00;\ 0.67$
Cloud-only CRE			
Mean bias ($\mathrm{W\,m^{-2}}$)	-	-1.22	-2.90
Function, R^2	$y = 8.22 \cdot x + 18.67;\ 0.61$	$y = 9.35 \cdot x + 16.14;\ 0.53$	$y = 10.33 \cdot x + 13.25;\ 0.36$

5.2 Thermal-infrared cloud radiative effects

In general, the calculation of the all-sky CRE from TIR imaging observations using a pixel-wise approach yields similar magnitudes of CRE as reported in existing literature (Fletcher et al., 2016b). Nevertheless, it has to be considered that here the broadband refers to the specific spectral range of the TIR atmospheric window from $7.7\,\mu\mathrm{m}$ to $12\,\mu\mathrm{m}$. For a direct comparison to the terrestrial CRE for the full spectral range from $3\,\mu\mathrm{m}$ to $100\,\mu\mathrm{m}$, this difference has to be considered. With radiative transfer simulations performed with libRadtran, this difference is quantified based on a selection of atmospheric profiles measured by dropsondes during the respective flights. For the weaker MCAO case, the difference between the terrestrial and thermal-infrared CRE is about $8.35\,\mathrm{W\,m^{-2}}$ while for the stronger event it is about $15.95\,\mathrm{W\,m^{-2}}$. As the CRE is defined here as the difference between the cloud-free and cloudy upward irradiance, use of the full spectral range is impacting both irradiances due to enhanced absorption outside the atmospheric window. The cloud-free irradiance is attenuated more strongly than the cloudy irradiance due to the warm ocean surface acting as an emission source and the longer pathway through the atmosphere. For the weak MCAO case, the clouds are lower and this imbalance between the states is therefore smaller compared to the stronger MCAO event.

https://doi.org/10.5194/egusphere-2026-5857
Preprint. Discussion started: 9 November 2026
© Author(s) 2026. CC BY 4.0 License.

Uncertainties concerning whether a pixel is truly cloud-free could also have an impact. For the strong MCAO event on 1 April 2022, it is not clear if a $100\,\%$ cloud-free pixel is present. The cloud fraction is generally high for this case and the upper threshold of the cloud mask is $-7.8\,^{\circ}\mathrm{C}$, which is rather low. For the cloud-free reference state needed to calculate the CREs, this is a crucial assumption. This potential underestimation of the cloud-free irradiance may have led to a general underestimation of the CREs. Thus, even as gaps between cloud streets visually appear to be cloud-free, there could still be traces of water vapor or humidified aerosol particles. Several studies already refer to these radiative effects close to cloud edges as the cloud transient zone (Eytan et al., 2020; Calbó et al., 2024). A coarser spatial sampling with spaceborne instrumentation might aggravate this challenge further.

6 Summary and conclusions

The TOA-like cloud radiative effects during a weak and a strong Arctic MCAO event are analyzed using airborne thermal-infrared imaging observations with high spatial resolution ($\sim 10\,\mathrm{m}$). A new threshold-based cloud mask is developed and applied, which discriminates between thin and thick cloud as well as cloud-free pixels. Based on the cloud mask, two types of CRE are calculated: the all-sky and cloud-only CRE, to separate the effects of cloud fraction and cloud properties (cloud emissivity and cloud top temperature). CREs and cloud fraction for the two MCAO cases are analyzed in their downstream development along trajectories. It is found that the downstream increase of the all-sky CRE is primarily driven by cloud fraction and that this relation is three times larger for the stronger MCAO event. The cloud-only CRE only increases weakly with time since sea ice indicating that the cloud properties do not change much.

Furthermore, the approach applicability and its sensitivity to the spatial resolution of the observations is tested. The airborne measurements are scaled down to the spatial resolutions of the EarthCARE MSI ($500\,\mathrm{m}$) and Terra/Aqua MODIS ($1000\,\mathrm{m}$) instruments. Differences in cloud fraction and CRE magnitude are identified. The strongest underestimations of the all-sky and cloud-only CRE are determined for the strong MCAO case at the MODIS resolution and are about $-1.9\,\mathrm{W\,m^{-2}}$ and $-2.9\,\mathrm{W\,m^{-2}}$, respectively. Nevertheless, similar relations between CREs and cloud fraction are found at all resolutions. However, reduced sampling of cloud and cloud-free features implies more uncertainty and less robustness of the conclusions. This particular point justifies the need for high-resolution spectral imaging of clouds in the Arctic.

The uncertainty analysis shows that the cloud mask is primarily sensitive to intermediate cloud fractions and its robustness for the extrema, i.e., cloud-free and opaque states. Challenges in the applied approach encompass contamination by sea ice and the definition of a cloud-free reference state. An analysis of the thin cloud class and its radiative effect would be a crucial next step for estimating the importance of cloud edges. The conclusions presented here are based on two MCAO cases. A statistical analysis of MCAO events of varying intensity would be a prospective extension of this study.

This analysis demonstrates that airborne TIR imaging can resolve tightly aligned cloud streets in MCAOs and that a pixel-wise calculation of CRE can assist in separating its driving factors. These conclusions are of importance for the frequently occurring MCAO events in winter during polar night. Due to their large spatial extent across longitudes and latitudes, the TOA CRE needs to be quantified by polar-orbiting satellites. These spatially coarser observations can benefit from validation

https://doi.org/10.5194/egusphere-2026-5857
Preprint. Discussion started: 9 November 2026
© Author(s) 2026. CC BY 4.0 License.

with the highly resolved and focused sampling strategies of airborne measurements. As a result, the impacts of these air mass transformation events for Arctic amplification and connected Arctic-mid-latitude linkages can be more accurately assessed, quantified, and parameterized in modelling frameworks.

Code and data availability. Two Jupyter notebooks are provided as supplementary material and contain the basic concept of the presented cloud mask and the cloud radiative effect calculation while reproducing Fig. 2 and Fig. 4. An overview of observational datasets collected during the HALO-$(\mathcal{AC})^3$ campaign can be found in Ehrlich et al. (2025). The VELOX brightness temperature fields are available at https://doi.org/10.1594/PANGAEA.963401 (Schäfer et al., 2023). The dropsonde profiles can be accessed at https://doi.pangaea.de/10.1594/PANGAEA.968891 (George et al., 2024). Aircraft position and attitude data are published on the HALO database (https://doi.org/10.17616/R39Q0T) at https://halo-db.pa.op.dlr.de/mission/130 (HALO Database, 2026). Backward trajectories are available upon request. An archive of AMSR2 sea ice concentration data can be accessed at https://seaice.uni-bremen.de/sea-ice-concentration/amsre-amsr2/ (Spreen et al., 2008).

Appendix A: Cloud mask sensitivity

The sensitivity of the cloud mask was analyzed by adding/subtracting the standard deviation (STD) to/from the mean thresholds (see Fig. 3). In total, four cases can be tested: adding the STD to the lower (lb) and upper boundary (ub) (+ STD lb and ub), subtracting from both (− STD lb and ub), and the two combinations (+ STD lb, − STD ub; − STD lb, + STD ub). The first two cases focus on a shift in thick cloud fraction and cloud-free fraction whereas the latter two add a shift in thin cloud fraction. Furthermore, the cloud-free reference is higher for + STD ub shifts and lower for − STD ub shifts. Figure A1 shows the relation of the CRE to the cloud fraction for these four changes in the cloud mask in comparison to using the mean thresholds as in Fig. 7. The two MCAO cases captured contrasting conditions with low cloud fractions during the weak MCAO and high cloud fractions during the strong MCAO. Therefore, the sensitivity of the CRE on the cloud mask can be tested for two regimes of cloud fractions separately.

For the all-sky CRE "+ STD lb and ub" and "− STD lb, + STD ub" (1) are the same, and "− STD lb and ub" and "+ STD lb, − STD ub" (2) are also the same. These pairs match because the result does not differ in the sum of thin and thick cloud fraction. Compared to using the mean thresholds, for (1) the cloud fraction is higher whereas (2) has a lower cloud fraction. Therefore, the all-sky CRE is shifted to higher/lower cloud fractions. For the strong MCAO event the linear functions describing pairs (1) and (2) converge with the linear function based on the mean thresholds at high cloud fractions. This intersection is expected given that the all-sky CRE should converge for opaque conditions that are clearly thick cloud, despite the threshold shifts. Similarly, a convergence is reached for low cloud fractions in the weak MCAO case, where cloud-free conditions dominate.

In contrast, the impact of the different thresholds on the cloud-only CRE is more complex because only the thick cloud pixels are considered. The "+ STD lb and ub" case also allows pixels with higher brightness temperatures to be classified as thick cloud, yielding a lower CRE for these pixels. The opposite effect can be observed for the "− STD lb and ub" case. The other two cases just change the total cloud fraction due to an additional change of the thin cloud fraction. A convergence is

https://doi.org/10.5194/egusphere-2026-5857
Preprint. Discussion started: 9 November 2026
© Author(s) 2026. CC BY 4.0 License.

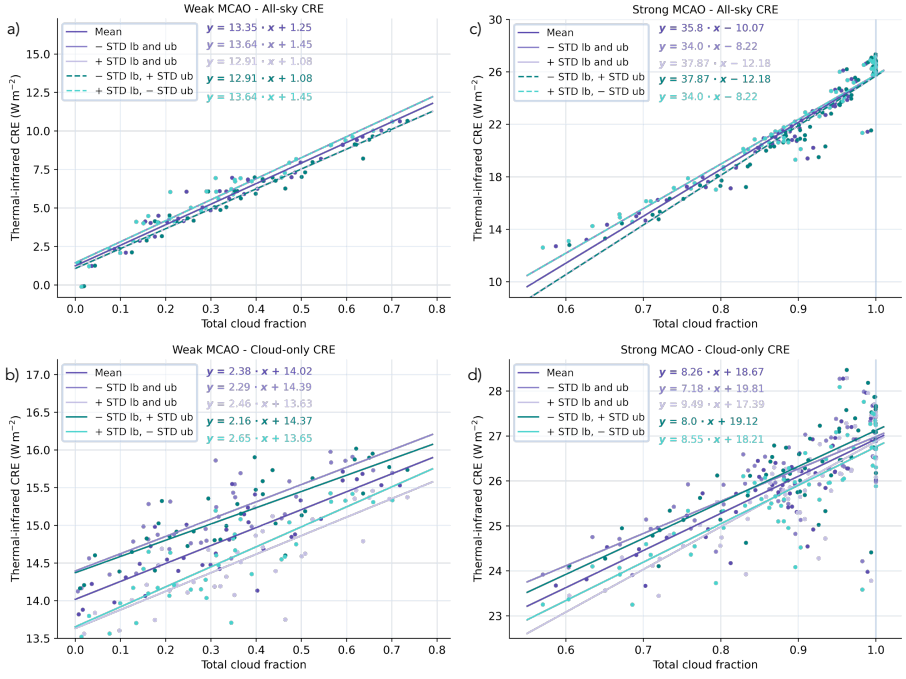


Figure A1. (a) and **(b)** mean all-sky/cloud-only CRE for the weak MCAO as a function of total cloud fraction (thin plus thick cloud fraction) for different variations of the cloud mask thresholds. Fitted linear functions are given. **(c)** and **(d)** same figures for the strong MCAO. Please be aware of the different axis scaling.

visible at higher cloud fractions. For low cloud fractions during the weak MCAO, the range of cloud-only CREs is wider due to sparsely occurring thick cloud pixels in their initial state (first hours since leaving the sea ice), which are not as homogeneous as those closed, thick cloud layers.

In conclusion, a convergence is expected in the cloud-only CRE for high cloud fractions due to the rather homogeneous cloud layers and a broader distribution for lower and intermediate cloud fractions. In this case, the fitted linear function is more dependent on the cloud mask thresholds.

For the all-sky CRE, only the range of intermediate cloud fractions is critical because at low (homogeneous ocean surface) and high cloud fractions (rather homogeneous closed cloud layers) the all-sky CRE is rather indifferent to slightly changing thresholds for the cloud mask. This also highlights the separation of high and low cloud fraction cases as two regimes that when analyzed independently can be constrained with a linear fit.

Finally, for the analysis of the relation between CREs and the cloud fraction, these variations do not change the initial linear function significantly. Deviations of slopes and intercepts are in the range of $1\,\mathrm{W\,m^{-2}}$ to $2\,\mathrm{W\,m^{-2}}$.

https://doi.org/10.5194/egusphere-2026-5857
Preprint. Discussion started: 9 November 2026
© Author(s) 2026. CC BY 4.0 License.

Author contributions. SR was the primary author of the paper. MW and AE designed the measurement campaign. BK, AL, MS, AE, MK, and MW conducted the airborne experimental work during the field campaign. MS, SR, and JM processed the VELOX data. BK performed the backward trajectory calculation. SR worked on the methodology, the analyses and drafted the article. All authors contributed to the discussion and presentation of results in this article.

Competing interests. The contact author has declared that none of the authors has any competing interests.

Acknowledgements. We gratefully acknowledge the funding by the Deutsche Forschungsgemeinschaft (DFG, German Research Foundation) – project number 268020496 – TRR 172, within the Transregional Collaborative Research Center "ArctiC Amplification: Climate Relevant Atmospheric and SurfaCe Processes, and Feedback Mechanisms $(\mathcal{AC})^3$". We also acknowledge the funding by the DFG within the Priority Program HALO SPP 1294 under project number 316646266. Special thanks to Johannes Röttenbacher who supported the provision of code and data. MODIS Terra Level 1B calibrated radiances with 1 km spatial resolution (product MOD021km; MODIS Science Team, 2024) datasets were acquired from the Level-1 & Atmosphere Archive and Distribution System (LAADS) Distributed Active Archive Center (DAAC), located in the Goddard Space Flight Center in Greenbelt, Maryland (https://ladsweb.modaps.eosdis.nasa.gov/). Parts of the results in this work make use of the colormaps in the CMasher package (van der Velden, 2020). This publication was supported by the Open Access Publishing Fund of Leipzig University.

https://doi.org/10.5194/egusphere-2026-5857
Preprint. Discussion started: 9 November 2026
© Author(s) 2026. CC BY 4.0 License.

References

Becker, S., Ehrlich, A., Schäfer, M., and Wendisch, M.: Airborne observations of the surface cloud radiative effect during different seasons over sea ice and open ocean in the Fram Strait, Atmos. Chem. Phys., 23, 7015–7031, https://doi.org/10.5194/acp-23-7015-2023, 2023.

Brümmer, B.: Boundary-layer modification in wintertime cold-air outbreaks from the Arctic sea ice, Bound.-Lay. Meteorol., 80, 109–125, https://doi.org/10.1007/BF00119014, 1996.

Brümmer, B.: Roll and Cell Convection in Wintertime Arctic Cold-Air Outbreaks, J. Atmos. Sci., 56, 2613–2636, https://doi.org/10.1175/1520-0469(1999)056<2613:RACCIW>2.0.CO;2, 1999.

Calbó, J., González, J.-A., Jahani, B., Sola, Y., and de Morales, J. R.: How important is the transition zone between clouds and aerosol?, AIP Conf. Proc., 2998, 070 005, https://doi.org/10.1063/5.0182769, 2024.

Chung, E.-S., Ha, K.-J., Timmermann, A., Stuecker, M. F., Bodai, T., and Lee, S.-K.: Cold–Season Arctic Amplification Driven by Arctic Ocean–Mediated Seasonal Energy Transfer, 9, https://doi.org/10.1029/2020EF001898, 2021.

Dahlke, S., Solbès, A., and Maturilli, M.: Cold Air Outbreaks in Fram Strait: Climatology, Trends, and Observations During an Extreme Season in 2020, J. Geophys. Res.-Atmos., 127, https://doi.org/10.1029/2021JD035741, 2022.

Dorff, H., Konow, H., and Ament, F.: Horizontal geometry of trade wind cumuli – aircraft observations from a shortwave infrared imager versus a radar profiler, Atmos. Meas. Tech., 15, 3641–3661, https://doi.org/10.5194/amt-15-3641-2022, 2022.

Ehrlich, A., Crewell, S., Herber, A., Klingebiel, M., Lüpkes, C., Mech, M., Becker, S., Borrmann, S., Bozem, H., Buschmann, M., Clemen, H.-C., de La Torre Castro, E., Dorff, H., Dupuy, R., Eppers, O., Ewald, F., George, G., Giez, A., Grawe, S., Gourbeyre, C., Hartmann, J., Jäkel, E., Joppe, P., Jourdan, O., Jurányi, Z., Kirbus, B., Lucke, J., Luebke, A. E., Maahn, M., Maherndl, N., Mallaun, C., Mayer, J., Mertes, S., Mioche, G., Moser, M., Müller, H., Pörtge, V., Risse, N., Roberts, G., Rosenburg, S., Röttenbacher, J., Schäfer, M., Schaefer, J., Schäfler, A., Schirmacher, I., Schneider, J., Schnitt, S., Stratmann, F., Tatzelt, C., Voigt, C., Walbröl, A., Weber, A., Wetzel, B., Wirth, M., and Wendisch, M.: A comprehensive in situ and remote sensing data set collected during the HALO-(AC)^3 aircraft campaign, Earth Syst. Sci. Data, 17, 1295–1328, https://doi.org/10.5194/essd-17-1295-2025, 2025.

Emde, C., Buras-Schnell, R., Kylling, A., Mayer, B., Gasteiger, J., Hamann, U., Kylling, J., Richter, B., Pause, C., Dowling, T., and Bugliaro, L.: The libRadtran software package for radiative transfer calculations (version 2.0.1), Geosci. Model Dev., 9, 1647–1672, https://doi.org/10.5194/gmd-9-1647-2016, 2016.

Eytan, E., Koren, I., Altaratz, O., Kostinski, A. B., and Ronen, A.: Longwave radiative effect of the cloud twilight zone, Nat. Geosci., 13, 669–673, https://doi.org/10.1038/s41561-020-0636-8, 2020.

Fletcher, J., Mason, S., and Jakob, C.: The Climatology, Meteorology, and Boundary Layer Structure of Marine Cold Air Outbreaks in Both Hemispheres*, J. Climate, 29, 1999–2014, https://doi.org/10.1175/JCLI-D-15-0268.1, 2016a.

Fletcher, J. K., Mason, S., and Jakob, C.: A Climatology of Clouds in Marine Cold Air Outbreaks in Both Hemispheres, J. Climate, 29, 6677–6692, https://doi.org/10.1175/JCLI-D-15-0783.1, 2016b.

George, G., Luebke, A. E., Klingebiel, M., Mech, M., and Ehrlich, A.: Dropsonde measurements from HALO and POLAR 5 during HALO-(AC)^3 in 2022, https://doi.org/10.1594/PANGAEA.968891, 2024.

Gryschka, M., Drüe, C., Etling, D., and Raasch, S.: On the influence of sea-ice inhomogeneities onto roll convection in cold-air outbreaks, Geophys. Res. Lett., 35, https://doi.org/10.1029/2008GL035845, 2008.

HALO Database: The High Altitude and LOng Range Research Aircraft Database, https://halo-db.pa.op.dlr.de/mission/130, last access: 20.08.2026, 2026.

https://doi.org/10.5194/egusphere-2026-5857
Preprint. Discussion started: 9 November 2026
© Author(s) 2026. CC BY 4.0 License.

Hersbach, H., Bell, B., Berrisford, P., Hirahara, S., Horányi, A., Muñoz-Sabater, J., Nicolas, J., Peubey, C., Radu, R., Schepers, D., Simmons, A., Soci, C., Abdalla, S., Abellan, X., Balsamo, G., Bechtold, P., Biavati, G., Bidlot, J., Bonavita, M., de Chiara, G., Dahlgren, P., Dee, D., Diamantakis, M., Dragani, R., Flemming, J., Forbes, R., Fuentes, M., Geer, A., Haimberger, L., Healy, S., Hogan, R. J., Hólm, E., Janisková, M., Keeley, S., Laloyaux, P., Lopez, P., Lupu, C., Radnoti, G., de Rosnay, P., Rozum, I., Vamborg, F., Villaume, S., and Thépaut, J.-N.: The ERA5 global reanalysis, Q. J. Roy. Meteor. Soc., 146, 1999–2049, https://doi.org/10.1002/qj.3803, 2020.

Juliano, T. W., Tornow, F., Fridlind, A. M., Ackerman, A. S., Elsaesser, G. S., Geerts, B., Lackner, C. P., Painemal, D., Silber, I., Ovchinnikov, M., Svensson, G., Tjernström, M., Wu, P., Baró Pérez, A., Bogenschutz, P., Chechin, D., Chandrakar, K. K., Chylik, J., Debolskiy, A., Fadeev, R., Gupta, A., Ickes, L., Karalis, M., Köhler, M., Kosović, B., Kuma, P., Li, W., Mortikov, E., Morrison, H., Neggers, R. A. J., Possner, A., Raatikainen, T., Raillard, L., Romakkaniemi, S., Schnierstein, N., Shima, S.-i., Silin, N., Tolstykh, M., Vignon, É., Xue, L., Zhang, M., and Zheng, X.: The Cold-Air Outbreaks in the Marine Boundary Layer Experiment model-observation intercomparison project (COMBLE-MIP) – Part 1: Model specification, observational constraints, and preliminary findings, Atmos. Chem. Phys., 26, 13 267–13 302, https://doi.org/10.5194/acp-26-13267-2026, 2026.

Kay, J. E., L'Ecuyer, T., Chepfer, H., Loeb, N., Morrison, A., and Cesana, G.: Recent Advances in Arctic Cloud and Climate Research, Curr. Clim. Change Rep., 2, 159–169, https://doi.org/10.1007/s40641-016-0051-9, 2016.

Kirbus, B., Schirmacher, I., Klingebiel, M., Schäfer, M., Ehrlich, A., Slättberg, N., Lucke, J., Moser, M., Müller, H., and Wendisch, M.: Thermodynamic and cloud evolution in a cold-air outbreak during HALO-$(AC)^3$: quasi-Lagrangian observations compared to the ERA5 and CARRA reanalyses, Atmos. Chem. Phys., 24, 3883–3904, https://doi.org/10.5194/acp-24-3883-2024, 2024.

Klingebiel, M., Ehrlich, A., Gryschka, M., Risse, N., Maherndl, N., Schirmacher, I., Rosenburg, S., Hörnig, S., Moser, M., Jäkel, E., Schäfer, M., Deneke, H., Mech, M., Voigt, C., and Wendisch, M.: Airborne observations of cloud properties during their evolution from organized streets to isotropic cloud structures along an Arctic cold-air outbreak, Atmos. Chem. Phys., 25, 9787–9801, https://doi.org/10.5194/acp-25-9787-2025, 2025.

Klingebiel, M., Luebke, A., Ehrlich, A., Mech, M., Sundermann, H., Deneke, H. M., Gryschka, M., Shupe, M. D., Zuidema, P., and Wendisch, M.: Observational Validation of Boundary-Layer Cloud Regimes in Arctic Cold Air Outbreaks, Wiley, [preprint], https://doi.org/10.22541/essoar.176599140.03217922/v2, 2026.

Kolstad, E. W.: Higher ocean wind speeds during marine cold air outbreaks, Q. J. Roy. Meteor. Soc., 143, 2084–2092, https://doi.org/10.1002/qj.3068, 2017.

Krautstrunk, M. and Giez, A.: The Transition From FALCON to HALO Era Airborne Atmospheric Research, in: Atmospheric Physics, edited by Schumann, U., Research topics in aerospace, pp. 609–624, Springer Berlin Heidelberg, Berlin, Heidelberg, ISBN 978-3-642-30182-7, https://doi.org/10.1007/978-3-642-30183-4_37, 2012.

Lackner, C. P., Geerts, B., Juliano, T. W., Xue, L., and Kosovic, B.: Vertical Structure of Clouds and Precipitation During Arctic Cold–Air Outbreaks and Warm–Air Intrusions: Observations From COMBLE, J. Geophys. Res.-Atmos., 128, https://doi.org/10.1029/2022JD038403, 2023.

Lloyd, G., Choularton, T. W., Bower, K. N., Gallagher, M. W., Crosier, J., O'Shea, S., Abel, S. J., Fox, S., Cotton, R., and Boutle, I. A.: In situ measurements of cloud microphysical and aerosol properties during the break-up of stratocumulus cloud layers in cold air outbreaks over the North Atlantic, Atmos. Chem. Phys., 18, 17 191–17 206, https://doi.org/10.5194/acp-18-17191-2018, 2018.

MODIS Science Team: MOD021KM MODIS/Terra Calibrated Radiances 5-Min L1B Swath 1km, https://doi.org/10.5067/MODIS/MOD021KM.007, 2024.

https://doi.org/10.5194/egusphere-2026-5857
Preprint. Discussion started: 9 November 2026
© Author(s) 2026. CC BY 4.0 License.

Morrison, H., de Boer, G., Feingold, G., Harrington, J., Shupe, M. D., and Sulia, K.: Resilience of persistent Arctic mixed-phase clouds, Nat. Geosci., 5, 11–17, https://doi.org/10.1038/ngeo1332, 2012.

Murray-Watson, R. J., Gryspeerdt, E., and Goren, T.: Investigating the development of clouds within marine cold air outbreaks, pp. 1–29, https://doi.org/10.5194/egusphere-2023-734, 2023.

Papritz, L. and Spengler, T.: A Lagrangian Climatology of Wintertime Cold Air Outbreaks in the Irminger and Nordic Seas and Their Role in Shaping Air–Sea Heat Fluxes, J. Climate, 30, 2717–2737, https://doi.org/10.1175/JCLI-D-16-0605.1, 2017.

Paulus, F. M., Müller, J. J., Kirbus, B., Sodemann, H., van Gelder, L., Walbröl, A., Wendisch, M., and Neggers, R. A. J.: Impacts of mesoscale atmospheric subsidence on cloud glaciation and decoupling in Arctic marine cold air outbreaks, https://doi.org/10.5194/egusphere-2026-554, 2026.

Pithan, F., Svensson, G., Caballero, R., Chechin, D., Cronin, T. W., Ekman, A. M. L., Neggers, R., Shupe, M. D., Solomon, A., Tjernström, M., and Wendisch, M.: Role of air-mass transformations in exchange between the Arctic and mid-latitudes, Nat. Geosci., 11, 805–812, https://doi.org/10.1038/s41561-018-0234-1, 2018.

Ran, H., Wang, L., Spengler, T., Chen, G., Huang, P., and Hu, K.: Long-Term Trends of Northern Hemisphere Marine Cold Air Outbreaks during Boreal Winter: Influence of Sea Ice Retreat and Atmospheric Circulation, J. Climate, 39, 2191–2207, https://doi.org/10.1175/JCLI-D-24-0658.1, 2026.

Schäfer, M., Wolf, K., Ehrlich, A., Hallbauer, C., Jäkel, E., Jansen, F., Luebke, A. E., Müller, J., Thoböll, J., Röschenthaler, T., Stevens, B., and Wendisch, M.: VELOX – a new thermal infrared imager for airborne remote sensing of cloud and surface properties, Atmos. Meas. Tech., 15, 1491–1509, https://doi.org/10.5194/amt-15-1491-2022, 2022.

Schäfer, M., Rosenburg, S., Ehrlich, A., Röttenbacher, J., and Wendisch, M.: Two-dimensional cloud-top and surface brightness temperature with 1 Hz temporal resolution derived at flight altitude from VELOX during the HALO-(AC)^3 field campaign, https://doi.org/10.1594/PANGAEA.963401, 2023.

Schirmacher, I., Schnitt, S., Klingebiel, M., Maherndl, N., Kirbus, B., Ehrlich, A., Mech, M., and Crewell, S.: Clouds and precipitation in the initial phase of marine cold-air outbreaks as observed by airborne remote sensing, Atmos. Chem. Phys., 24, 12 823–12 842, https://doi.org/10.5194/acp-24-12823-2024, 2024.

Schyberg, H., X., Y., M.A.Ø., K., Amstrup B., Bakketun, Å., Bazile, E., Bojarova, J., Box, J. E., Dahlgren, P., H. S., Homleid, M., Horányi, A., Høyer, J., Johansson, Å., Killie, M., Körnich, H., Le Moigne, P., Lindskog, M., Manninen, T., Nielsen Englyst, P., Nielsen, K., Olsson, E., Palmason, B., Peralta Aros, C., Randriamampianina, R., Samuelsson, P., Stappers, R., Støylen, E., Thorsteinsson, S., Valkonen, T., and Wang, Z.: Arctic regional reanalysis on single levels from 1991 to present, https://doi.org/10.24381/CDS.713858F6, 2021a.

Schyberg, H., Yang, X., Køltzow, M., Amstrup, B., Bakketun, Å., Bazile, E., Bojarova, J., Box, J. E., Dahlgren, P., Hagelin, S., Homleid, M., Horányi, A., Høyer, J., Johansson, Å., Killie, M., Körnich, H., Le Moigne, P., Lindskog, M., Manninen, T., Nielsen Englyst, P., Nielsen, K., Olsson, E., Palmason, B., Peralta Aros, C., Randriamampianina, R., Samuelsson, P., Stappers, R., Støylen, E., Thorsteinsson, S., Valkonen, T., and Wang, Z.: Arctic regional reanalysis on pressure levels from 1991 to present, https://doi.org/10.24381/CDS.E3C841AD, 2021b.

Sedlar, J., Shupe, M. D., and Tjernström, M.: On the Relationship between Thermodynamic Structure and Cloud Top, and Its Climate Significance in the Arctic, J. Climate, 25, 2374–2393, https://doi.org/10.1175/JCLI-D-11-00186.1, 2012.

Shupe, M. D. and Intrieri, J. M.: Cloud Radiative Forcing of the Arctic Surface: The Influence of Cloud Properties, Surface Albedo, and Solar Zenith Angle, J. Climate, 17, 616–628, https://doi.org/10.1175/1520-0442(2004)017<0616:CRFOTA>2.0.CO;2, 2004.

Spensberger, C. and Spengler, T.: Sensitivity of Air–Sea Heat Exchange in Cold–Air Outbreaks to Model Resolution and Sea–Ice Distribution, J. Geophys. Res.-Atmos., 126, https://doi.org/10.1029/2020JD033610, 2021.

https://doi.org/10.5194/egusphere-2026-5857
Preprint. Discussion started: 9 November 2026
© Author(s) 2026. CC BY 4.0 License.

Spreen, G., Kaleschke, L., and Heygster, G.: Sea ice remote sensing using AMSR–E 89–GHz channels, J. Geophys. Res.-Oceans, 113, https://doi.org/10.1029/2005JC003384, 2008.

Sprenger, M. and Wernli, H.: The LAGRANTO Lagrangian analysis tool – version 2.0, Geosci. Model Dev., 8, 2569–2586, https://doi.org/10.5194/gmd-8-2569-2015, 2015.

Stevens, B., Ament, F., Bony, S., Crewell, S., Ewald, F., Gross, S., Hansen, A., Hirsch, L., Jacob, M., Kölling, T., Konow, H., Mayer, B., Wendisch, M., Wirth, M., Wolf, K., Bakan, S., Bauer-Pfundstein, M., Brueck, M., Delanoë, J., Ehrlich, A., Farrell, D., Forde, M., Gödde, F., Grob, H., Hagen, M., Jäkel, E., Jansen, F., Klepp, C., Klingebiel, M., Mech, M., Peters, G., Rapp, M., Wing, A. A., and Zinner, T.: A High-Altitude Long-Range Aircraft Configured as a Cloud Observatory: The NARVAL Expeditions, B. Am. Meteorol. Soc., 100, 1061–1077, https://doi.org/10.1175/BAMS-D-18-0198.1, 2019.

van der Velden, E.: CMasher: Scientific colormaps for making accessible, informative and 'cmashing' plots, The Journal of Open Source Software, 5, 2004, https://doi.org/10.21105/joss.02004, 2020.

Weber, A., Kirbus, B., Wendisch, M., and Mayer, B.: Quasi-Lagrangian observations of cloud transitions during the initial phase of marine cold air outbreaks in the Arctic - Part 1: Temporal and spatial evolution, Atmos. Chem. Phys., 26, 3521–3540, https://doi.org/10.5194/acp-26-3521-2026, 2026.

Webster, P. J.: The role of hydrological processes in ocean–atmosphere interactions, Rev. Geophys., 32, 427–476, https://doi.org/10.1029/94RG01873, 1994.

Wehr, T., Kubota, T., Tzeremes, G., Wallace, K., Nakatsuka, H., Ohno, Y., Koopman, R., Rusli, S., Kikuchi, M., Eisinger, M., Tanaka, T., Taga, M., Deghaye, P., Tomita, E., and Bernaerts, D.: The EarthCARE mission – science and system overview, Atmos. Meas. Tech., 16, 3581–3608, https://doi.org/10.5194/amt-16-3581-2023, 2023.

Wendisch, M., Brückner, M., Crewell, S., Ehrlich, A., Notholt, J., Lüpkes, C., Macke, A., Burrows, J. P., Rinke, A., Quaas, J., Maturilli, M., Schemann, V., Shupe, M. D., Akansu, E. F., Barrientos-Velasco, C., Bärfuss, K., Blechschmidt, A.-M., Block, K., Bougoudis, I., Bozem, H., Böckmann, C., Bracher, A., Bresson, H., Bretschneider, L., Buschmann, M., Chechin, D. G., Chylik, J., Dahlke, S., Deneke, H., Dethloff, K., Donth, T., Dorn, W., Dupuy, R., Ebell, K., Egerer, U., Engelmann, R., Eppers, O., Gerdes, R., Gierens, R., Gorodetskaya, I. V., Gottschalk, M., Griesche, H., Gryanik, V. M., Handorf, D., Harm-Altstädter, B., Hartmann, J., Hartmann, M., Heinold, B., Herber, A., Herrmann, H., Heygster, G., Höschel, I., Hofmann, Z., Hölemann, J., Hünerbein, A., Jafariserajehlou, S., Jäkel, E., Jacobi, C., Janout, M., Jansen, F., Jourdan, O., Jurányi, Z., Kalesse-Los, H., Kanzow, T., Käthner, R., Kliesch, L. L., Klingebiel, M., Knudsen, E. M., Kovács, T., Körtke, W., Krampe, D., Kretzschmar, J., Kreyling, D., Kulla, B., Kunkel, D., Lampert, A., Lauer, M., Lelli, L., von Lerber, A., Linke, O., Löhnert, U., Lonardi, M., Losa, S. N., Losch, M., Maahn, M., Mech, M., Mei, L., Mertes, S., Metzner, E., Mewes, D., Michaelis, J., Mioche, G., Moser, M., Nakoudi, K., Neggers, R., Neuber, R., Nomokonova, T., Oelker, J., Papakonstantinou-Presvelou, I., Pätzold, F., Pefanis, V., Pohl, C., van Pinxteren, M., Radovan, A., Rhein, M., Rex, M., Richter, A., Risse, N., Ritter, C., Rostosky, P., Rozanov, V. V., Donoso, E. R., Saavedra Garfias, P., Salzmann, M., Schacht, J., Schäfer, M., Schneider, J., Schnierstein, N., Seifert, P., Seo, S., Siebert, H., Soppa, M. A., Spreen, G., Stachlewska, I. S., Stapf, J., Stratmann, F., Tegen, I., Viceto, C., Voigt, C., Vountas, M., Walbröl, A., Walter, M., Wehner, B., Wex, H., Willmes, S., Zanatta, M., and Zeppenfeld, S.: Atmospheric and Surface Processes, and Feedback Mechanisms Determining Arctic Amplification: A Review of First Results and Prospects of the $(AC)^3$ Project, B. Am. Meteorol. Soc., 104, E208–E242, https://doi.org/10.1175/BAMS-D-21-0218.1, 2023.

Wendisch, M., Crewell, S., Ehrlich, A., Herber, A., Kirbus, B., Lüpkes, C., Mech, M., Abel, S. J., Akansu, E. F., Ament, F., Aubry, C., Becker, S., Borrmann, S., Bozem, H., Brückner, M., Clemen, H.-C., Dahlke, S., Dekoutsidis, G., Delanoë, J., de La Torre Castro, E., Dorff, H., Dupuy, R., Eppers, O., Ewald, F., George, G., Gorodetskaya, I. V., Grawe, S., Groß, S., Hartmann, J., Henning, S., Hirsch, L., Jäkel,

https://doi.org/10.5194/egusphere-2026-5857
Preprint. Discussion started: 9 November 2026
© Author(s) 2026. CC BY 4.0 License.

E., Joppe, P., Jourdan, O., Jurányi, Z., Karalis, M., Kellermann, M., Klingebiel, M., Lonardi, M., Lucke, J., Luebke, A. E., Maahn, M., Maherndl, N., Maturilli, M., Mayer, B., Mayer, J., Mertes, S., Michaelis, J., Michalkov, M., Mioche, G., Moser, M., Müller, H., Neggers, R., Ori, D., Paul, D., Paulus, F. M., Pilz, C., Pithan, F., Pöhlker, M., Pörtge, V., Ringel, M., Risse, N., Roberts, G. C., Rosenburg, S., Röttenbacher, J., Rückert, J., Schäfer, M., Schaefer, J., Schemann, V., Schirmacher, I., Schmidt, J., Schmidt, S., Schneider, J., Schnitt, S., Schwarz, A., Siebert, H., Sodemann, H., Sperzel, T., Spreen, G., Stevens, B., Stratmann, F., Svensson, G., Tatzelt, C., Tuch, T., Vihma, T., Voigt, C., Volkmer, L., Walbröl, A., Weber, A., Wehner, B., Wetzel, B., Wirth, M., and Zinner, T.: Overview: quasi-Lagrangian observations of Arctic air mass transformations – introduction and initial results of the HALO–(AC)^3 aircraft campaign, Atmos. Chem. Phys., 24, 8865–8892, https://doi.org/10.5194/acp-24-8865-2024, 2024.

Wendisch, M., Kirbus, B., Ori, D., Shupe, M. D., Crewell, S., Sodemann, H., and Schemann, V.: Observed and modeled Arctic airmass transformations during warm air intrusions and cold air outbreaks, Atmos. Chem. Phys., 25, 15 047–15 076, https://doi.org/10.5194/acp-25-15047-2025, 2025.

Xia, Z. and McFarquhar, G. M.: Dependence of Cloud Macrophysical Properties and Phase Distributions on Environmental Conditions Over the North Atlantic and Southern Ocean: Results From COMBLE and MARCUS, J. Geophys. Res.-Atmos., 129, https://doi.org/10.1029/2023JD039869, 2024.